Tailored synthesis of $NdMn_xFe_{1-x}O_3$ perovskite nanoparticles with oxygen-vacancy defects for lithium-ion battery anodes

Anh Tien Nguyen [a,1], Thanh Ngoc Nguyen [b,1], Valentina Olegovna Mittova [c], Quang Quoc Viet Thieu [d], Irina Yakovlevna Mittova [e], Van Man Tran [f,g,h], Minh Thu Nguyen [g,h], Dinh Quan Nguyen [h,i], Il Tae Kim [j,**], Tuan Loi Nguyen [k,l,*]

[a] Faculty of Chemistry, Ho Chi Minh City University of Education, Ho Chi Minh City, 700000, Viet Nam
[b] NTT Hi-Tech Institute, Nguyen Tat Thanh University, 300A Nguyen Tat Thanh Street, Ho Chi Minh City, Viet Nam
[c] Scientific-Research Institute of Experimental and Clinical Medicine, Teaching University Geomedi LLC, Tbilisi, 0114, Georgia
[d] Faculty of Chemical Engineering, College of Engineering, Can Tho University, Campus II, 3/2 Street, Ninh Kieu District, Can Tho City, Viet Nam
[e] Department of Materials Science and Industry of Nanosystems, Faculty of Chemistry, Voronezh State University, Voronezh, 394018, Russian Federation
[f] Department of Physical Chemistry, Faculty of Chemistry, VNUHCM-University of Science, Viet Nam
[g] Applied Physical Chemistry Laboratory (APCLAB), VNUHCM-University of Science, Viet Nam
[h] Vietnam National University Ho Chi Minh City, Linh Trung Ward, Thu Duc District, Ho Chi Minh City, Viet Nam
[i] Laboratory of Biofuel and Biomass Research, Faculty of Chemical Engineering, Ho Chi Minh City University of Technology (HCMUT), 268 Ly Thuong Kiet Street, District 10, Ho Chi Minh City, Viet Nam
[j] Department of Chemical and Biological Engineering, Gachon University, Seongnam-si, Gyeonggi-do, 13120, Republic of Korea
[k] Institute of Fundamental and Applied Sciences, Duy Tan University, Ho Chi Minh City, 700000, Viet Nam
[l] Faculty of Environmental and Chemical Engineering, Duy Tan University, Da Nang City, 550000, Viet Nam

ARTICLE INFO

ABSTRACT

In this study, we synthesize nanostructured $NdMn_xFe_{1-x}O_3$ perovskites using a facile method to produce materials for the high-working-efficiency anodes of Li-ion batteries. A series of characterization assessments (e.g., X-ray diffraction (XRD), X-ray photoelectron spectroscopy (XPS), and electron microscopy) were conducted, and the results confirmed the efficacious partial replacement of Fe ions with Mn ions in the $NdFeO_3$ perovskite structure, occurrence of both amorphous and crystalline structures, presence of oxygen vacancies (V_O), and interconnection between nanoparticles. The possibility of Mn ion replacement significantly affects the size, amount of V_O, and ratio of amorphous phase in $NdMn_xFe_{1-x}O_3$ perovskites. The $NdMn_xFe_{1-x}O_3$ perovskite with x = 0.3 presents a notable electrochemical performance, including low charge transfer resistance, durable Coulombic efficiency, first-rate capacity reservation, high pseudo-behavior, and elongated 150-cycle service life, whereas no discernible capacity deterioration is observed. The reversible capacity of the anode after the 150th-cylcle was 713 mAh g^{-1}, which represents a high-capacity value. The outstanding electrochemical efficiency resulted from the optimum presence of V_O, interconnection between the nanoparticles, and distinctive properties of the $NdFeO_3$ perovskite. The interconnection between nanoparticles was advantageous for forming a large electrolyte-electrode contact area, improving Li-ion diffusion rates, and enhancing

---

* Corresponding author. Institute of Fundamental and Applied Sciences, Duy Tan University, Ho Chi Minh City 700000, Viet Nam.
** Corresponding author.
  E-mail addresses: itkim@gachon.ac.kr (I.T. Kim), nguyentuanloi@duytan.edu.vn (T.L. Nguyen).
[1] These authors contributed equally to this work.

pseudocapacitive effect. The attributes of perovskite crystals, coexistence of Mn and Fe throughout the charge/discharge process, and optimum V_O precluded the electrode devastation that caused the Li_2O-phase decomposition catalysis, enabling favorable reversible Li storage.

1. Introduction

In the context of climate change threatening the survival of all creatures, net-zero CO_2 emissions become the global mission of all countries and the goal of manufacturing industry. Especially in car and motorbike manufacturing, engines using fossil fuels have been gradually replaced by engines using greener and cleaner energy sources. Lithium-ion batteries (LIBs) are the preference in the design of new vehicle and electronic device generations. They have advantages such as an elevated working voltage, a prolonged life, an elevated energy density, an absence of memory effect, and a low self-discharge [1–5]. Therefore, LIBs have been exploited as electrochemical energy storage devices for modern electronic devices. Graphite is the best universal anode material for LIBs; however, graphite anodes suffer from serious unavoidable problems such as inadequate theoretical capacity (~372 mAh g^{-1}) and near-lithium-plating operating voltage, which leads to low energy density and unsafe LIBs using graphite anodes [6,7]. To meet the market demand for LIBs, new anode materials that exhibit superior capacity, high safety, and impressive cycling constancy to replace graphite in commercial LIB anodes need to be studied and developed [8–10]. Metal oxides have been attractive candidates for replacing graphite anodes due to their safety, large capacity, broad availability, and low processing cost. For instance, a novel hybrid nanostructure was developed by exploiting coating of amorphous carbon around $CoSnO_3$ nanoboxes using controlled hydrothermal carbonization of glucose. The resulted hybrid nanostructure exhibited a tremendously long cycle life of over 400 cycles and enhanced high-rate capability. However, a large capacity loss in the first cycle occurred due to initial irreversible formation of Li_2O and other irreversible processes [11]. Efforts have been made to produce a variety of nanocomposites of graphene nanosheets/Sn-based to improve the volume changes of conventional Sn-based anodes, enhancing them to be more applicable [8]. In the composites of SnO_2 with graphene sheets, the synergistic effect between SnO_2 and graphene can effectively improve the anode's storage capacity. Nevertheless, it is the challenge to achieve the best parameters for preparing SnO_2/graphene nanocomposites with good cycle performance, high specific capacity, and high rate performance [9].

Perovskite materials have been emerging anode materials for new generations of LIBs as they shows noticeable advantages such as the ease of synthesis and structure modification and durability of layer structure [12]. This type of materials, however, exhibits unsatisfactory lithium-ion storage capacity [12–15]. Thus, there is an urgent need to discover new perovskite materials as active electrode candidates for portable energy storage devices.

Over the past several decades, ferrite perovskites and analogous compounds have been considered the most promising materials for energy conversion/storage systems caused by their unique complex function-performing ability [16–18]. Recently, $NdFeO_3$ perovskite (ABO_3 perovskite structure) has been utilized as an anode material in LIBs; however, a high capacity is yet to be achieved. For example, perovskite-structured $Nd_{0.7}Co_{0.3}FeO_3$ nanoparticles (NPs) were successfully synthesized using a facile hydrothermal method, and this perovskite could deliver a capacity of 291 mAh g^{-1} after 100th cycles when utilized as an anode material in LIBs [19]. Interestingly, Nguyen et al. prepared $NdFeO_3$ perovskites with nanostructures as anodes for LIBs using a coprecipitation technique, in which a reversible capacity of 475 mAh g^{-1} was delivered after the 450th cycle at 100 mA g^{-1} [15]. In recent years, Hu et al. developed $NdFeO_3$ nanofibers using an electrospinning technique, which delivered only an initial capacity of 337 mAh g^{-1} at 200 mA g^{-1} as the anode for LIBs [20].

The $NdFeO_3$ perovskite possesses a distorted orthorhombic structure where Nd^{3+} and Fe^{3+} occupy positions A and B, respectively. A unit cell with a distorted orthorhombic structure was formed from an octahedral structure centered on Fe^{3+} in the FeO_3 cavity and enclosed by Nd^{3+} ions in the lattice. To improve the electrochemical performance of the $NdFeO_3$ perovskite anode, metal (Mn) doping into the B-site of the $NdFeO_3$ perovskite to form the $NdMn_xFe_{1-x}O_3$ perovskite at the nanoscale was investigated in this study. Based on this idea, nanostructured $NdMn_xFe_{1-x}O_3$ materials were designed using a simple coprecipitation technique. The efficacious partial replacement of Fe ions with Mn ions in the $NdFeO_3$ perovskite could lead to the formation of many oxygen vacancies (V_O), as well as the co-existence of cations such as Fe^{3+}, Fe^{2+}, Mn^{3+}, and Mn^{2+}. When applied to the anodes of LIBs, $NdMn_xFe_{1-x}O_3$ NPs with x = 0.3 posed notable electrochemical performances with a high retention capacity, notable current rate, and excellent Coulombic efficiency (CE).

2. Material and methods

2.1. Chemical synthesis

The chemicals used for the fabrication of $NdMn_xFe_{1-x}O_3$ (x = 0.1, 0.3, and 0.5) nanomaterials were $Fe(NO_3)_3 \cdot 9H_2O$ (99.6 %, Sigma-Aldrich, USA), $Nd(NO_3)_3 \cdot 6H_2O$ (99.8 %, Merck, Germany), $Mn(NO_3)_2 \cdot xH_2O$ (98 %), NaOH (97 %), deionized (DI) water, and phenolphthalein test paper. No further reagent purification was performed.

2.2. Synthesis of the $NdMn_xFe_{1-x}O_3$ material

Following the coprecipitation method, nanosized $NdMn_xFe_{1-x}O_3$ powders (x = 0.1, 0.3, and 0.5) were synthesized using steps

similar to those described in other studies [21,22]. A solution containing $Nd(NO_3)_3$, $Mn(NO_3)_2$, and $Fe(NO_3)_3$ at an appropriate molar ratio in a total volume of 50 mL was gradually added dropwise into 450 mL of boiling DI water under continuous stirring. The resulting solution was boiled at 100 °C for 5 min and cooled down to ~27 °C. Redundant cations (Nd^{3+}, Fe^{3+}, Mn^{2+}) were precipitated using 5 % NaOH droplets, and a phenolphthalein indicator was utilized simultaneously to indicate the terminating point of the reaction. The precipitate was stirred thoroughly for 45 min and filtered under vacuum. The washing step was repeated using DI water until the pH reached 7. The precipitate was dried naturally at room temperature (~27 °C) and ground thoroughly. The ground reddish-brown powder was further processed via annealing at 800 °C for 1 h under air conditions at a constant heating rate of 10 K min^{-1}. The resulting powder was the $NdMn_xFe_{1-x}O_3$ perovskite, which was ready for application as an anode in LIBs.

2.3. Material characterization

XRD analysis (Cu Kα) was operated for the crystal structure determination of synthesized nanomaterials. The surface morphology and composition of $NdMn_xFe_{1-x}O_3$ were analyzed using transmission electron microscopy (TEM), XPS, energy-dispersive X-ray spectroscopy (EDS), and high-resolution TEM (HRTEM).

2.4. Electrochemical performance measurements

The anode was fabricated as follows: $NdMn_xFe_{1-x}O_3$, Super P, and poly(acrylic acid) binder with mass compositions of 70, 15, and 15 %, respectively, were thoroughly mixed in ethanol to create a homogeneous slurry. Then, the resulting slurry was pasted onto a copper foil to form a current-collecting structure. The slurry-coated Cu foils were dried at 70 °C overnight under vacuum. A battery grade 1.0 M $LiPF_6$ solution in a solvent mixture composed of diethyl carbonate and ethylene carbonate (volume ratio of 50:50) was used as the electrolyte. Counter and reference electrodes were made of lithium metal, and the separator was made of Celgard 2400 films. Subsequently, a half-cell assembly was performed in an argon-filled glove box, and the working electrode was constructed from a $NdMn_xFe_{1-x}O_3$ coated foil.

With the support of Arbin Instruments (LBT20084), cyclic voltammetry (CV) assays of the assembled half-cell were conducted (scan rate = 0.3 mV s^{-1} and voltage range = 0.01–3.00 V). The CV measurements were performed at various sweep speeds (0.3–1.2 mV s^{-1}) with the voltage ranging between 0.01 and 3.00 V for studying the diffusion coefficients of lithium ions as well as anode kinetics. Galvanostatic cycling was performed at 0.1 A g^{-1} using a battery cycle tester (Neware) (voltage span of 0.01–3.00 V). The current rate capacities were measured under various current rates (0.1, 0.2, 0.5, 1.0, and 3.0 A g^{-1}). Electrochemical impedance spectroscopy (EIS) measurements were conducted using a Gamry instrument (1010E) over a large frequency range of 1 MHz to 0.1 Hz.

3. Results and discussion

Several chemical reactions occur during the synthesis of the novel perovskite. First, metal hydroxyls ($Fe(OH)_3$, $Mn(OH)_2$, and $Nd(OH)_3$) were formed by the reactions of metal cations (i.e., Fe^{3+}, Mn^{2+}, and Nd^{3+}) with the hydroxyl groups derived from NaOH, as described in

$$Fe^{3+} + 3\ OH^- \rightarrow Fe(OH)_3 \downarrow \tag{1}$$

$$Mn^{2+} + 2\ OH^- \rightarrow Mn(OH)_2 \downarrow \tag{2}$$

$$Nd^{3+} + 3\ OH- \rightarrow Nd(OH)_3 \downarrow \tag{3}$$

After filtration and drying at room temperature, these metal hydroxyls underwent a 1 h ambient heating process in a furnace at
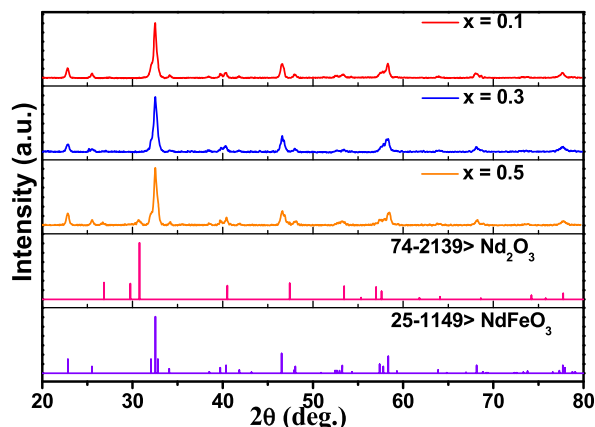

Fig. 1. XRD patterns of $NdMn_xFe_{1-x}O_3$ powders with x = 0.1, 0.3, and 0.5.

800 °C to produce H_2O and $NdMn_xFe_{1-x}O_3$ powders, as shown in

$$2(1-x)\ Fe(OH)_3 + 2x\ Mn(OH)_2 + 2\ Nd(OH)_3 + \tfrac{1}{2}\ x\ O_2 \rightarrow 2\ NdMn_xFe_{1-x}O_3 + (6-x)\ H_2O \uparrow \tag{4}$$
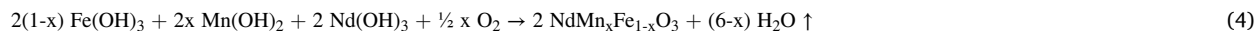
Fig. 1 illustrates the XRD patterns of the $NdMn_xFe_{1-x}O_3$ NPs and reference patterns of Nd_2O_3 and $NdFeO_3$. Fig. 1 confirms that, when the x value increased from 0.1 to 0.3, the XRD spectra of the $NdMn_xFe_{1-x}O_3$ NPs were well-fitted with the reference patterns of the $NdFeO_3$ phase (PDF#25–1149). The radii of Fe^{3+} ions and Mn^{3+} ions at a high spin state are similar (0.645 Å), and consequently,

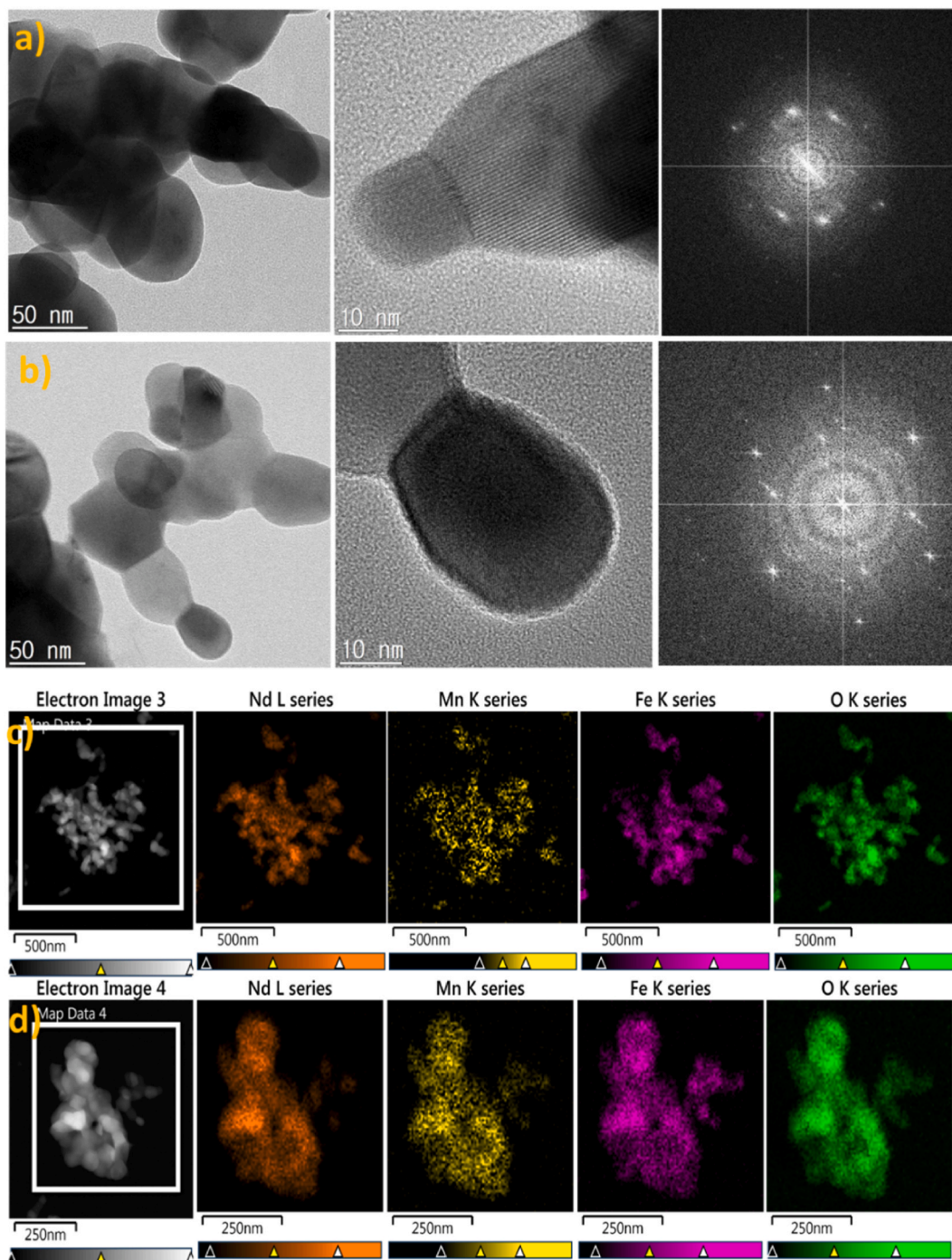**Fig. 2.** TEM, HRTEM and SAED images of $NdMn_xFe_{1-x}O_3$ NPs with (a) x = 0.1 and (b) x = 0.3. EDS mapping images of $NdMn_xFe_{1-x}O_3$ NPs with (c) x = 0.1 and (d) x = 0.3.

the unit cell of $NdFeO_3$ is not affected by the replacements of Fe^{3+} ions by Mn^{3+} ions. When x was 0.5, the XRD pattern showed the existence of both $NdFeO_3$ (PDF#25–1149) and Nd_2O_3 phases (PDF#74–2139), indicating that Fe^{3+} ions by Mn^{3+} ions successfully occurred. The spectra of all $NdMn_xFe_{1-x}O_3$ samples contained many broad and sharp peaks, indicating the presence of both amorphous and crystalline structures, as confirmed by the selected area electron diffraction (SAED) images.

The size, morphology, structure, and composition of the $NdMn_xFe_{1-x}O_3$ samples are evaluated using TEM, HRTEM, SAED, and EDS analyses (Fig. 2). As displayed in Fig. 2a-b, TEM and HRTEM graphs exhibit NP sizes ranging from 30 to 60 nm and interconnections between NPs, whereas the HRTEM and SAED graphs reveal the appearance of amorphous and crystalline structures, which is consistent with the XRD results. Interconnected NPs can help enhance the contact area between the electrolyte and electrodes and reduce the diffusion length of Li^+ ions, which results in enhanced electrochemical properties. For x from 0.1 to 0.3, there were decreases in NP sizes while the amorphous phase fractions grew (Fig. 2a-b); this can be attributed to the different formations of V_O and cations in the $NdMn_xFe_{1-x}O_3$ perovskites when increasing the concentration of Mn^{2+} ions. Fig. 2c-d show the EDS mapping images of the $NdMn_xFe_{1-x}O_3$ powders, which verify the co-presence and homogeneous distribution of Mn, Fe, Nd, and O in the $NdMn_xFe_{1-x}O_3$ perovskites. The elemental compositions (Mn, Fe, Nd, and O) of $NdMn_xFe_{1-x}O_3$ perovskites are presented in Table 1.

The valence states of the elements and presence of V_O in the $NdMn_xFe_{1-x}O_3$ samples were further studied using XPS. Fig. 3a and c show the survey profiles of the $NdMn_xFe_{1-x}O_3$ samples with x = 0.1 and x = 0.3, which denote the existence of Nd, Mn, Fe, and O elements. In Fig. 3b and d, the peaks of Nd 3d appear at 982 eV and 1004.7 eV, which correspond to the Nd $3d_{5/2}$ and Nd $3d_{3/2}$ orbitals of Nd^{3+}, respectively [23–25].

The Fe 2p spectra are separated into six peaks as shown in Fig. 4a–d. The two peaks positioned at 725.3 eV and 711.9 eV are ascribed to $2p_{1/2}$ and $2p_{3/2}$ of Fe^{3+}, respectively. The other two peaks located at 723.8 eV and 710.6 eV can be correlated to $2p_{1/2}$ and $2p_{3/2}$ of Fe^{2+}, respectively [26,27]. Finally, the two weak peaks at 719 and 733 eV were satellite peaks [28], which suggest the existence of both Fe^{3+} and Fe^{2+} in the $NdMn_xFe_{1-x}O_3$ particles. As shown in Fig. 4b–e, the high-resolution Mn 2p spectra show two zones consisting of Mn $2p_{1/2}$ (at 652.7 eV) and Mn $2p_{3/2}$ (at 641.5 eV), which can be divided into four peaks. The peaks at 641.24 eV and 652.12 eV are attributed to the binding energy of Mn^{2+}; the others at 644.81 and 653.13 eV reveal the Mn^{3+} existence [29]. For O 1s, the fitting curves (Fig. 4c–f) are separated into two discrete peaks at 529 eV and 531.3 eV. The one at 529 eV can be contributed by M−O (M = Nd, Fe, Mn) bonds [20,30–32]. The peak detected at 531.3 eV could be the result of the V_O occurrence inside $NdMn_xFe_{1-x}O_3$ particles [29,33–36]. In the spectra of O 1s, the estimation of the area ratio between V_O and M−O showed the result of 1.98 and 1.66 for $NdMn_xFe_{1-x}O_3$ NPs with x = 0.1 and x = 0.3, respectively. The amount of V_O in the x = 0.1 sample was higher than that in the x = 0.3 sample. The XPS results confirm that the partial replacement of Fe ions by Mn ions in the $NdFeO_3$ perovskite structure leads to the formation of Mn^{2+}, Mn^{3+}, and Fe^{2+} cations and V_O. The presence of V_O with an appropriate amount can help increase the ionic conductivity, alleviate volume expansion, and bring about active site abundance, which leads to improved electrochemical performance [37–40].

The electrochemical properties of the $NdMn_xFe_{1-x}O_3$ electrodes were examined by CV over the 0.01–3.00 V potential range with a defined sweep rate of 0.3 mV s^{-1}. As shown in Fig. 5(a-b), a broad peak between 1 V and 0.01 V was obtained in the initial cathodic scan of $NdMn_xFe_{1-x}O_3$ electrodes, indicating the conversion process of $NdMn_xFe_{1-x}O_3$ (Eq. (5)) and the growth of a layer called the solid electrolyte interphase (SEI) [28,41]. The first CV curve of the cathodic scan is opposite to that of the subsequent cycles, which reveals that provocation occurred in the first cycle. Interestingly, the peak intensities increased in the later cycles, confirming the continuous activation of $NdMn_xFe_{1-x}O_3$ that improved the cycle life performance capacity. The remaining peaks in the subsequent cycles were the result of conversion/reconversion reactions between $Fe^{3+}/Nd^{3+}/Mn^{3+}/Mn^{2+}/Fe^{2+}$ and $Fe^0/Nd^0/Mn^0$ (Eq. (5) and Eq. (6)).

Peaks emerging in the anodic and cathodic scans for $NdMn_xFe_{1-x}O_3$ with x = 0.1 and x = 0.3 varied slightly because of the divergent amount of Mn (Table 1). The CVs of the $NdMn_xFe_{1-x}O_3$ electrode with x = 0.1 show a cathodic/anodic peak at 0.78/1.56 V (Fig. 5a), which is ascribed to the conversion/reconversion reactions of Fe^{3+}, Fe^{2+}, Mn^{2+} and Mn^{3+} [41–43], while the CVs of the $NdMn_xFe_{1-x}O_3$ electrode with x = 0.3 revealed two cathodic/anodic peaks at 0.55/1.63 V and 0.82/2.06 V (Fig. 5b). The ratio of Mn in the $NdMn_xFe_{1-x}O_3$ NPs with x = 0.1 is approximately 3.8 times lower than that in the $NdMn_xFe_{1-x}O_3$ NPs with x = 0.3 (Table 1); hence, the peaks associated with the conversion/reconversion reaction of Mn^{2+}/Mn^{3+} in the case of x = 0.1 overlapped with the peak resulting from the conversion/reconversion reactions of Fe^{2+}/Fe^{3+}. As shown in Fig. 5b, there are 0.82 V and 0.55 V peaks in the cathodic scans because of the conversion reactions of $Fe^{3+}/Fe^{2+}/Mn^{3+}/Mn^{2+}$ to form Fe^0/Mn^0, and two anodic peaks at 1.63 V and 2.06 V that could be related to the reconversion reactions of Fe^0/Mn^0 to yield $Fe^{3+}/Fe^{2+}/Mn^{2+}/Mn^{3+}$ [1,41–44].

$$NdMn_xFe_{1-x}O_3 + 6\ Li^+ + 6\ e^- \rightarrow 3\ Li_2O + Nd + (1-x)\ Fe + xMn \tag{5}$$

$$3\ Li_2O + Nd + (1-x)\ Fe + x\ Mn \rightarrow NdMn_xFe_{1-x}O_3 + 6\ Li^+ + 6\ e^- \tag{6}$$

Fig. 5c shows the charge–discharge potential performance of the $NdMn_xFe_{1-x}O_3$ anodes during the initial cycle. The $NdMn_xFe_{1-x}O_3$ electrode with the x = 0.1 delivered charge/discharge capacities of 352/616 mAh g^{-1}, consequently causing an initial Coulombic

Table 1
EDS analysis results for the $NdMn_xFe_{1-x}O_3$ perovskites.

	% Atom
x = 0.1	Nd: Mn: Fe: O = 18.22 : 1.55: 11.31 : 68.91
x = 0.3	Nd: Mn: Fe: O = 17.09 : 5.90: 10.04 : 66.97

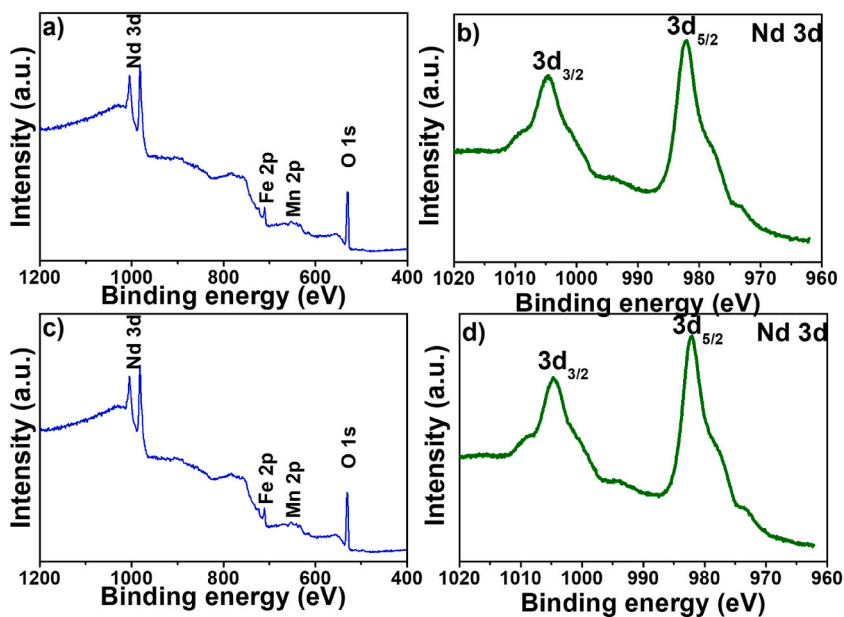**Fig. 3.** Survey spectra and high-resolution XPS of **Nd 3d** for NdMn$_x$Fe$_{1-x}$O$_3$ with (a–b) x = 0.1, and (c–d) x = 0.3.

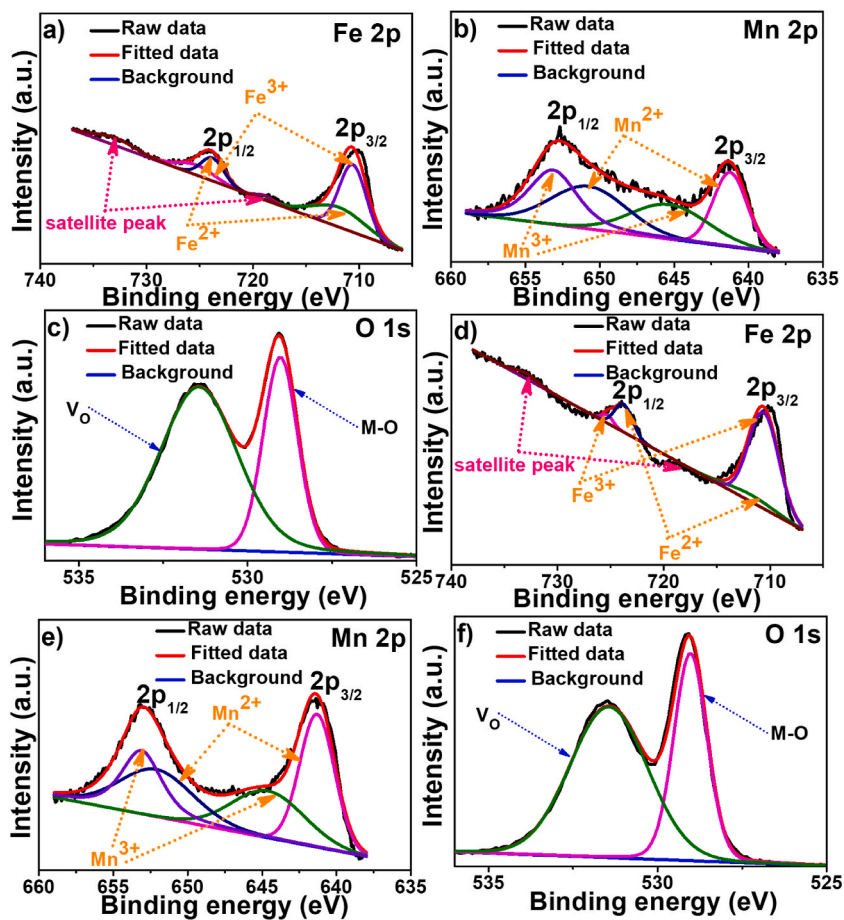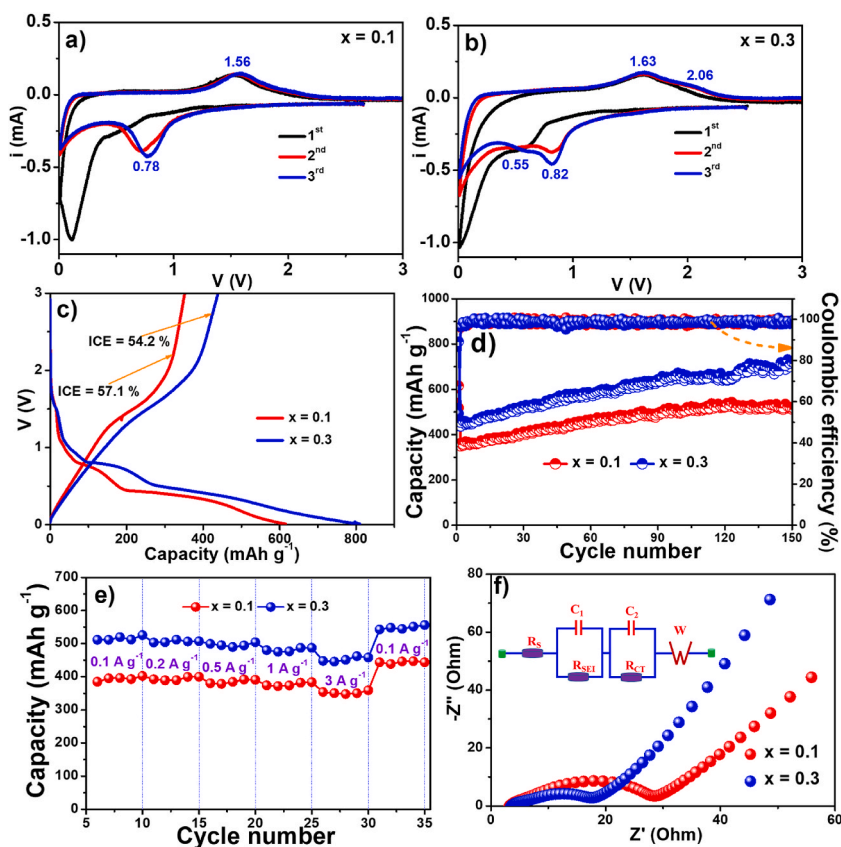**Fig. 4.** High-resolution XPS spectra of **Fe 2p**, **Mn 2p**, and **O 1s** for NdMn$_x$Fe$_{1-x}$O$_3$ NPs with (a–c) x = 0.1, and (d–f) x = 0.3.

Fig. 5. CV curves of $NdMn_xFe_{1-x}O_3$ electrodes with (a) x = 0.1 and (b) x = 0.3. (c) Charge-discharge profiles in the first cycles, (d) cycle performance, (e) rate capability of $NdMn_xFe_{1-x}O_3$ anodes. (f) Nyquist plot after rate test of $NdMn_xFe_{1-x}O_3$ anodes.

efficiency (ICE) of 57.1 %. The $NdMn_xFe_{1-x}O_3$ electrode with x = 0.3 possessed charge/discharge capacities of 439/810 mAh g^{-1}, initiating an ICE of 54.2 %. The variation in the formation of the SEI layer during the initial cycling may be the main reason for the ICE diversity of the $NdMn_xFe_{1-x}O_3$ electrodes. Fig. 5c shows that the capacities of the $NdMn_xFe_{1-x}O_3$ electrodes are boosted when increasing x values from 0.1 to 0.3; in contrast, the ICE declines, which can be related to the weight change of the active components (Table 1), different amount of V_O, and smaller nanoparticle size in the $NdMn_xFe_{1-x}O_3$ NPs with x = 0.3. Therefore, amplified capacity and SEI layer formation were observed.

Fig. 5d illustrates the working cycle profile and CE of $NdMn_xFe_{1-x}O_3$ anodes. In the first cycle, a low CE was achieved because of the SEI formation; afterwards, it rapidly climbed in the subsequent cycles and reached more than 98.6 % only after three cycles. The charge capacities of the $NdMn_xFe_{1-x}O_3$ electrodes increased significantly from 352 mAh g^{-1} (x = 0.1) and 439 mAh g^{-1} (x = 0.3) in the first cycle to 511 mAh g^{-1} (x = 0.1) and 713 mAh g^{-1} (x = 0.3) in the 150th cycle. The corresponding capacity retentions are 145 % (x = 0.1) and 162 % (x = 0.3). The capacity increase during cycling can be attributed to more than a few phenomenon, i.e., polymeric gel-like film development [45,46], charge storage side reactions [47], nanoparticle refinement [48], porous material activation [49,50], and the function of the nanosized Mn and Fe metals in the perovskite structure as active substances for Li_2O constituent decay during continuous cycling [51–55]. When considering the cycling properties, the anode with x = 0.3 represents a higher capacity than that with x = 0.1, even though the anode with x = 0.1 had a higher value of V_O. This indicates the presence of an appropriate amount of V_O for better electrochemical performance. The amount of V_O has a positive effect on capacity; however, the existence of a large amount of

Table 2
Comprehensive comparison of ferrite perovskite anodes for LIBs.

Ferrite perovskite anodes	Current density (mA g^{-1})	Cycling number	Capacity (mAh g^{-1})	Reference
$NdFeO_3$	100	450	460	[15]
$HoFeO_3$	100	100	428	[12]
$Nd_{0.7}Co_{0.3}FeO_3$	500	100	291	[19]
$NdFeO_3$ NFs	200	500	467	[20]
$LaFeO_3$	100	200	331	[59]
$NdMn_xFe_{1-x}O_3$	*100*	*150*	*713*	*In this work*

V_O can result in the loss of many O (metal oxides) in the structure, which decreases capacity [30,56–58]. In addition, $NdMn_xFe_{1-x}O_3$ NPs with x = 0.3 had a small size compared to $NdMn_xFe_{1-x}O_3$ NPs with x = 0.1 (Fig. 2), which results in the enhanced electrochemical properties of the anode with x = 0.3. The electrochemical characteristics of the $NdMn_xFe_{1-x}O_3$ electrode (x = 0.3) matched the foregoing reports on ferrite perovskite-based electrodes, showing outstanding performance, as presented in Table 2. It is noted that the as-prepared $NdMn_xFe_{1-x}O_3$ electrode (x = 0.3) exhibited higher capacity with high stability (Fig. 5d) compared to several ferrite perovskite anodes (Table 2). The anode with high capacity has a significant benefit regarding energy density. This study demonstrates one viable research to overcome the low capacity of existing graphite anodes. To realize long-distance travel with a single charge, it is necessary that the anode has high capacity with greatly stable cycling. When combining a cathode with the as-developed anode, a stable full cell with high energy density could be achieved. In this regard, a future work to fabricate a high-energy-density full cell can be conducted by applying the $NdMn_xFe_{1-x}O_3$ electrode as well as by modulating some parameters such as N/P ratio and cut-off voltages.

Fig. 5e and Fig. S1 show that the $NdMn_xFe_{1-x}O_3$ electrode (x = 0.3) performed an overwhelming rate capability compared to x = 0.1 and x = 0.5. The $NdMn_xFe_{1-x}O_3$ electrode with the x = 0.3 electrode possessed charge capacities of 516, 507, 497, 481, and 453 mAh g^{-1} at 100, 200, 500, 1000, and 3000 mA g^{-1}, which indicates the capacity retentions of 100, 98.1, 96.2, 93.2, and 87.7 %, respectively. The charge capacity of 549 mAh g^{-1} was achieved and the corresponding capacity reservation rate was 106.3 % because the current density was curtailed back to 100 mA g^{-1}, demonstrating the enhanced rate capability of the $NdMn_xFe_{1-x}O_3$ anode with x = 0.3. This enhancement is caused by the higher number of active sites, appropriate amount of V_O, and shortened Li^+ diffusion pathway resulting from the perovskite structures and interconnected NPs. The outstanding performance of the $NdMn_xFe_{1-x}O_3$ perovskite can be explained by the nano refinement effect occurring in the particles, contribution of nano-sized Mn and Fe metals, appropriate amount of V_O, interconnected NPs, and exceptional structure of the perovskite. This enhances the Li^+ diffusion rate and prevents electrode deterioration during the working stage.

The EIS assays of $NdMn_xFe_{1-x}O_3$ electrodes were performed to better explain the excellent rate capability of these anodes, as shown in Fig. 5f. The electrode Nyquist plots consisted of two semicircular arcs in the high- and medium-frequency regions and a sharp straight line in the remaining zone. This matches the ohmic resistance of the separator, electrolyte, and battery terminal, which leads to the physical resistance (R_e), charge-transfer resistance (R_{CT}), and SEI layer resistance (R_{SEI}) [60–62]. The $NdMn_xFe_{1-x}O_3$ anode with x = 0.3 displayed lower R_{CT} and R_{SEI} values than those of the $NdMn_xFe_{1-x}O_3$ anode with x = 0.1, as shown in Table 3. Low R_{SEI} and R_{CT} values indicate excellent characteristics such as the prolonged SEI layer stability, curtailed ion transport path length, and high structural durability of the perovskite during the charge/discharge process. These characteristics could result from the partial replacement of Fe^{3+} ions by Mn^{3+} and Mn^{2+} ions, interconnected NPs as well as the existence of V_O in the $NdMn_xFe_{1-x}O_3$ nano perovskite.

For kinetic assessment, the pseudo and diffusive profiles of the prepared electrodes were obtained at every scan rate based on the CV curves (Fig. 6(a-b)), Eq. S1, and solving matrix S2. The curves at every scan rate were well divided into pseudo-and diffusive curves by mathematically solving the matrix S3 (Fig. S2 and Fig. S3). Fig. 6c-d presents the involvement proportions of the diffusive and pseudo processes in the $NdMn_xFe_{1-x}O_3$ electrodes. The proportion of pseudo processes in the $NdMn_xFe_{1-x}O_3$ electrodes were always above 77 %, which reveals the surface-level electrochemical reactions. At the same scan rate, the pseudo process involvement proportion for the $NdMn_xFe_{1-x}O_3$ one (with x = 0.1) was larger than that in the case of $NdMn_xFe_{1-x}O_3$ one (with x = 0.3); this difference was smaller than 2 % (Fig. 6d). These minor differences could be related to the size diversity and different amounts of V_O in the $NdMn_xFe_{1-x}O_3$ nanomaterials with different x values (Fig. 2a-b). To observe the large difference between the electrodes, the kinetics of $NdMn_xFe_{1-x}O_3$ electrode (with x = 0.5) were also investigated as shown in Fig. S4 and Fig. S5. It is interesting that in the case of x = 0.5, the proportion of pseudo processes were always below 46 % (Fig. S5b). These results indicate that the kinetics tend to change from surface-controlled to diffusion-controlled when increasing x values from 0.3 to 0.5. Therefore, it can draw a conclusion that the partial replacement of Fe ions by Mn ions leads to a significant effect on the electrochemical kinetic process. Fig. 6c-d shows that the pseudo capacitance increased with an increase in the scan rate. This results in fast battery charge and discharge. The results were consistent with those of the cell efficiency, rate capacity, and EIS investigations.

4. Conclusion

A facile method was applied to successfully replace part of the Fe^{3+} ion composition with Mn^{2+}/Mn^{3+} ions for synthesizing orthorhombic $NdMn_xFe_{1-x}O_3$ nano perovskites consisting of V_O. The $NdMn_xFe_{1-x}O_3$ perovskite with x = 0.3 as the LIB anode exhibited extraordinarily improved electrochemical properties such as low charge transfer resistance, excellent CE, overwhelming capacity reservation, prolonged 150-cycle life with no considerable performance degradation, and great pseudo-capacitance. The $NdMn_xFe_{1-x}O_3$ perovskite with x = 0.3 revealed a good cyclic performance with a capacity of 713 mAh g^{-1} after 150 cycles at 100 mA g^{-1} and a charge capacity of 453 mAh g^{-1} at 3000 mA g^{-1}.

Table 3
EIS analysis results for $NdMn_xFe_{1-x}O_3$ electrodes.

	x = 0.1	x = 0.3
R_S (Ω)	3.5	3.8
R_{SEI} (Ω)	3.8	2.9
R_{CT} (Ω)	17.5	7.7
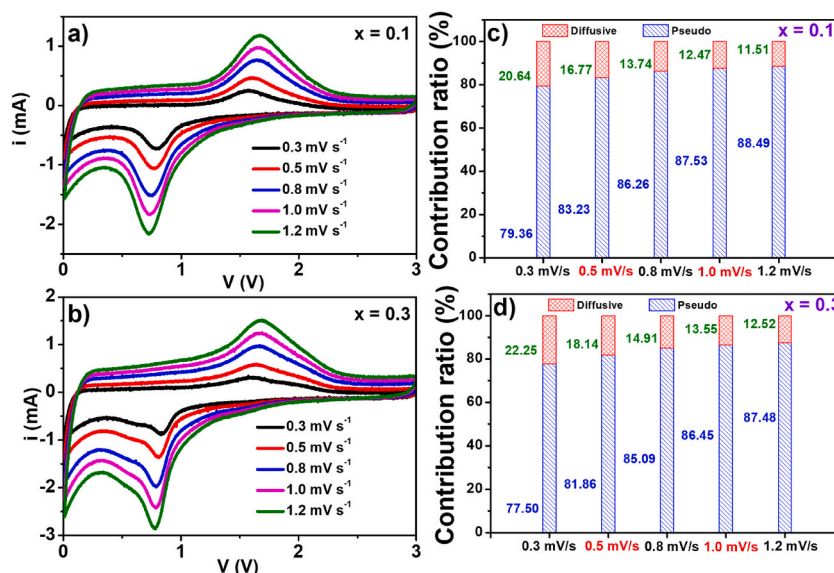
Fig. 6. CV plots of NdMn$_x$Fe$_{1-x}$O$_3$ anode at several scan rates after 2 cycles with (a) x = 0.1 and (b) x = 0.3. Diffusion-controlled and pseudo-capacitive involvement at altered scanning rates of NdMn$_x$Fe$_{1-x}$O$_3$ anodes with (c) x = 0.1 and (d) x = 0.3.

There are several reasons for the electrochemical property enhancement of NdMn$_x$Fe$_{1-x}$O$_3$ perovskites as active anode materials: (1) the curtailed Li-ion diffusion path length and enlarged electrolyte–electrode interface resulting from the nano-size and inter-connectivity of the electrode-material; (2) the distinctive structural advantages of ferrite perovskites and oxygen-vacancy defects counteract electrode devastation in cycling period, which brings about an excellently reversible storage; (3) the presence of nanoscale metal-catalysts (Mn and Fe) for the Li$_2$O-phase breakdown throughout charge/discharge, which produces a superb reversible capacity. The discovery in the present study proves that this novel and facile manufacturing method can be applied to the mass production of perovskite materials for high-quality lithium-storage facilities.

CRediT authorship contribution statement

Anh Tien Nguyen: Investigation, Methodology. **Thanh Ngoc Nguyen:** Writing – original draft. **Valentina Olegovna Mittova:** Formal analysis, Methodology. **Quang Quoc Viet Thieu:** Validation, Writing – original draft. **Irina Yakovlevna Mittova:** Validation, Visualization. **Van Man Tran:** Resources. **Minh Thu Nguyen:** Methodology, Resources. **Dinh Quan Nguyen:** Formal analysis, Resources. **Il Tae Kim:** Supervision, Writing – original draft. **Tuan Loi Nguyen:** Conceptualization, Writing – original draft.

Declaration of competing interest

The authors declare the following financial interests/personal relationships which may be considered as potential competing interests:Il Tae Kim reports a relationship with Heliyon that includes: board membership.

Appendix A. Supplementary data

Supplementary data to this article can be found online at https://doi.org/10.1016/j.heliyon.2023.e21782.

References

[1] B. Yue, Q. Hu, L. Ji, Y. Wang, J. Liu, Facile synthesis of perovskite CeMnO$_3$ nanofibers as an anode material for high performance lithium-ion batteries, RSC Adv. 9 (2019) 38271–38279.
[2] M. Fang, X. Yao, W. Li, Y. Li, M. Shui, J. Shu, The investigation of lithium doping perovskite oxide LiMnO$_3$ as possible LIB anode material, Ceram. Int. 44 (2018) 8223–8231.
[3] M. Li, X. Xiao, Y. Liu, W. Zhang, Y. Zhang, L. Chen, Ternary perovskite cobalt titanate/graphene composite material as long-term cyclic anode for lithium-ion battery, J. Alloys Compd. 700 (2017) 54–60.
[4] M. Armand, J.-M. Tarascon, Building better batteries, Nature 451 (2008) 652–657.
[5] B. Dunn, H. Kamath, J.-M. Tarascon, Electrical energy storage for the grid: a battery of choices, Science 334 (2011) 928–935.
[6] J. Ma, F. Yu, Z. Wen, M. Yang, H. Zhou, C. Li, L. Jin, L. Zhou, L. Chen, Z. Yuan, A facile one-pot method for synthesis of low-cost iron oxide/activated carbon nanotube electrode materials for lithium-ion batteries, Dalton Trans. 42 (2013) 1356–1359.

[7] R.M. Humana, M.G. Ortiz, J.E. Thomas, S.G. Real, M. Sedlarikova, J. Vondrák, A. Visintin, Preparation and characterization of graphite anode for lithium ion batteries, ECS Trans. 63 (2014) 91.

[8] Y. Zhao, X. Li, B. Yan, D. Li, S. Lawes, X. Sun, Significant impact of 2D graphene nanosheets on large volume change tin-based anodes in lithium-ion batteries: a review, J. Power Sources 274 (2015) 869–884.

[9] Y. Deng, C. Fang, G. Chen, The developments of SnO_2/graphene nanocomposites as anode materials for high performance lithium ion batteries: a review, J. Power Sources 304 (2016) 81–101.

[10] N. Nitta, F. Wu, J.T. Lee, G. Yushin, Li-ion battery materials: present and future, Mater. Today 18 (2015) 252–264.

[11] Z. Wang, Z. Wang, W. Liu, W. Xiao, X.W.D. Lou, Amorphous $CoSnO_3$@C nanoboxes with superior lithium storage capability, Energy Environ. Sci. 6 (2013) 87–91.

[12] A.T. Nguyen, V.D. Phung, V.O. Mittova, H.D. Ngo, T.N. Vo, M.L. Le Thi, I.Y. Mittova, M.L.P. Le, Y.N. Ahn, I.T. Kim, Fabricating nanostructured $HoFeO_3$ perovskite for lithium-ion battery anodes via co-precipitation, Scripta Mater. 207 (2022), 114259.

[13] G.-M. Weng, J. Kong, H. Wang, C. Karpovich, J. Lipton, F. Antonio, Z.S. Fishman, H. Wang, W. Yuan, A.D. Taylor, A highly efficient perovskite photovoltaic-aqueous Li/Na-ion battery system, Energy Storage Mater. 24 (2020) 557–564.

[14] J. Yan, D. Wang, X. Zhang, J. Li, Q. Du, X. Liu, J. Zhang, X. Qi, A high-entropy perovskite titanate lithium-ion battery anode, J. Mater. Sci. 55 (2020) 6942–6951.

[15] A.T. Nguyen, T.-A. Nguyen, V.O. Mittova, H.D. Ngo, M.L.P. Le, D.Q. Nguyen, I.Y. Mittova, V.H. Nguyen, S. Hiroshi, H.T. Bui, Facile co-precipitated synthesis of $NdFeO_3$ perovskite nanoparticles for lithium-ion battery anodes, J. Mater. Sci. Mater. Electron. 33 (2022) 19082–19091.

[16] P. Tan, M. Liu, Z. Shao, M. Ni, Recent advances in perovskite oxides as electrode materials for nonaqueous lithium–oxygen batteries, Adv. Energy Mater. 7 (2017), 1602674.

[17] J. Young, J.M. Rondinelli, Octahedral rotation preferences in perovskite iodides and bromides, J. Phys. Chem. Lett. 7 (2016) 918–922.

[18] M. Pena, J. Fierro, Chemical structures and performance of perovskite oxides, Chem. Rev. 101 (2001) 1981–2018.

[19] K. Ogunniran, G. Murugadoss, R. Thangamuthu, P. Periasamy, Evaluation of nanostructured $Nd_{0.7}Co_{0.3}FeO_3$ perovskite obtained via hydrothermal method as anode material for Li-ion battery, Mater. Chem. Phys. 248 (2020), 122944.

[20] Q. Hu, B. Yue, W. Su, D. Yang, Y. Wang, X. Dong, D. Liu, Syntheses, characterization, magnetic, and electrical properties of perovskite-type $NdFeO_3$ and $NdCoO_3$ nanofibers, J. Am. Ceram. Soc. 105 (2022) 6732–6743.

[21] N.T.K. Chung, N.A. Tien, C.H. Diem, B.X. Vuong, Structural and optical properties of Sr-doped $NdFeO_3$ nanoparticles prepared by a simple co-precipitation method, J. Chem. Sci. 134 (2022) 34.

[22] T.A. Nguyen, T.L. Pham, I.Y. Mittova, V.O. Mittova, T.L.T. Nguyen, H.V. Nguyen, V.X. Bui, Co-doped $NdFeO_3$ nanoparticles: synthesis, optical, and magnetic properties study, Nanomaterials 11 (2021) 937.

[23] X. Li, Z. Cao, H. Yue, Q. Wang, H. Zhang, S.-T. Yang, Tuning primary particle growth of $Li_{1.2}Ni_{0.2}Mn_{0.6}O_2$ by Nd-modification for improving the electrochemical performance of lithium ion batteries, ACS Sustain. Chem. Eng. 7 (2019) 5946–5952.

[24] S. Wang, Y. Li, S. Liu, S. Deng, Y. Chen, J. Zhu, J. Zhang, J. Guo, S. Chang, Superior electrochemical and kinetics performance of $LiNi_{0.8}Co_{0.15}Al_{0.05}O_2$ cathode by neodymium synergistic modifying for lithium ion batteries, J. Electrochem. Soc. 167 (2020), 090509.

[25] J. Kujawa, S. Al-Gharabli, G. Wrzeszcz, K. Knozowska, R. Lagzdins, E. Talik, A. Dziedzic, P. Loulergue, A. Szymczyk, W. Kujawski, Physicochemical and magnetic properties of functionalized lanthanide oxides with enhanced hydrophobicity, Appl. Surf. Sci. 542 (2021), 148563.

[26] Q. An, F. Lv, Q. Liu, C. Han, K. Zhao, J. Sheng, Q. Wei, M. Yan, L. Mai, Amorphous vanadium oxide matrixes supporting hierarchical porous Fe_3O_4/graphene nanowires as a high-rate lithium storage anode, Nano Lett. 14 (2014) 6250–6256.

[27] A.G. Nene, M. Takahashi, P.R. Somani, Fe_3O_4 and Fe nanoparticles by chemical reduction of $Fe(acac)_3$ by ascorbic acid: role of water, World J. Nano Sci. Eng. 6 (2016) 20.

[28] Q. Ai, Z. Yuan, R. Huang, C. Yang, G. Jiang, J. Xiong, Z. Huang, S. Yuan, One-pot co-precipitation synthesis of Fe_3O_4 nanoparticles embedded in 3D carbonaceous matrix as anode for lithium ion batteries, J. Mater. Sci. 54 (2019) 4212–4224.

[29] Z. Fang, M. Xu, Q. Li, M. Qi, T. Xu, Z. Niu, N. Qu, J. Gu, J. Wang, D. Wang, Over-reduction-controlled mixed-valent manganese oxide with tunable Mn^{2+}/Mn^{3+} ratio for high-performance asymmetric supercapacitor with enhanced cycling stability, Langmuir 37 (2021) 2816–2825.

[30] T.L. Nguyen, T.N. Vo, V.D. Phung, K. Ayalew, D. Chun, A.T. Luu, Q.H. Nguyen, K.J. Kim, I.T. Kim, J. Moon, Li-ion storage in orthorhombic hydrated sodium molybdate with oxygen-vacancy defects, Chem. Eng. J. 446 (2022), 137174.

[31] B.V.R. Reddy, R. Ravikumar, C. Nithya, S. Gopukumar, High performance Na_xCoO_2 as a cathode material for rechargeable sodium batteries, J. Mater. Chem. A 3 (2015) 18059–18063.

[32] A.A. Bortoti, A. de Freitas Gavanski, Y.R. Velazquez, A. Galli, E.G. de Castro, Facile and low cost oxidative conversion of MoS_2 in α-MoO_3: synthesis, characterization and application, J. Solid State Chem. 252 (2017) 111–118.

[33] Y. Jeong, C. Bae, D. Kim, K. Song, K. Woo, H. Shin, G. Cao, J. Moon, Bias-stress-stable solution-processed oxide thin film transistors, ACS Appl. Mater. Interfaces 2 (2010) 611–615.

[34] T. Szörényi, L. Laude, I. Bertoti, Z. Kantor, Z. Geretovszky, Excimer laser processing of indium-tin-oxide films: an optical investigation, J. Appl. Phys. 78 (1995) 6211–6219.

[35] P.-T. Hsieh, Y.-C. Chen, K.-S. Kao, C.-M. Wang, Luminescence mechanism of ZnO thin film investigated by XPS measurement, Appl. Phys. A 90 (2008) 317–321.

[36] U.T.T. Doan, A.T.T. Pham, T.B. Phan, S. Park, A.T. Luu, Q.H. Nguyen, T.S. Lo, T.D. Tap, M. Ohtani, N.K. Pham, Abnormal volatile and normal stable bipolar resistive switching characteristics of hybrid nanocomposites: morphology–defects–property 'Relationship, J. Alloys Compd. 857 (2021), 157602.

[37] Y. Zhang, L. Tao, C. Xie, D. Wang, Y. Zou, R. Chen, Y. Wang, C. Jia, S. Wang, Defect engineering on electrode materials for rechargeable batteries, Adv. Mater. 32 (2020), 1905923.

[38] S. Wang, L. Li, W. He, Y. Shao, Y. Li, Y. Wu, X. Hao, Oxygen vacancy modulation of bimetallic oxynitride anodes toward advanced Li-ion capacitors, Adv. Funct. Mater. 30 (2020), 2000350.

[39] C. Hou, Y. Hou, Y. Fan, Y. Zhai, Y. Wang, Z. Sun, R. Fan, F. Dang, J. Wang, Oxygen vacancy derived local build-in electric field in mesoporous hollow Co_3O_4 microspheres promotes high-performance Li-ion batteries, J. Mater. Chem. A 6 (2018) 6967–6976.

[40] N. Li, K. Du, G. Liu, Y. Xie, G. Zhou, J. Zhu, F. Li, H.-M. Cheng, Effects of oxygen vacancies on the electrochemical performance of tin oxide, J. Mater. Chem. A 1 (2013) 1536–1539.

[41] Q. Wu, R. Zhao, X. Zhang, W. Li, R. Xu, G. Diao, M. Chen, Synthesis of flexible Fe_3O_4/C nanofibers with buffering volume expansion performance and their application in lithium-ion batteries, J. Power Sources 359 (2017) 7–16.

[42] J.Z. Wang, C. Zhong, D. Wexler, N.H. Idris, Z.X. Wang, L.Q. Chen, H.K. Liu, Graphene-encapsulated Fe_3O_4 nanoparticles with 3D laminated structure as superior anode in lithium ion batteries, Chem. Eur J. 17 (2011) 661–667.

[43] L. Wang, J. Wu, Y. Chen, X. Wang, R. Zhou, S. Chen, Q. Guo, H. Hou, Y. Song, Hollow nitrogen-doped Fe_3O_4/carbon nanocages with hierarchical porosities as anode materials for lithium-ion batteries, Electrochim. Acta 186 (2015) 50–57.

[44] X. Gu, J. Yue, L. Li, H. Xue, J. Yang, X. Zhao, General synthesis of MnO_x (MnO_2, Mn_2O_3, Mn_3O_4, MnO) hierarchical microspheres as lithium-ion battery anodes, Electrochim. Acta 184 (2015) 250–256.

[45] W. Zhang, X. Li, J. Liang, K. Tang, Y. Zhu, Y. Qian, One-step thermolysis synthesis of two-dimensional ultrafine Fe_3O_4 particles/carbon nanonetworks for high-performance lithium-ion batteries, Nanoscale 8 (2016) 4733–4741.

[46] Y. Zhong, L. Su, M. Yang, J. Wei, Z. Zhou, Rambutan-like $FeCO_3$ hollow microspheres: facile preparation and superior lithium storage performances, ACS Appl. Mater. Interfaces 5 (2013) 11212–11217.

[47] H. Kim, W. Choi, J. Yoon, J.H. Um, W. Lee, J. Kim, J. Cabana, W.-S. Yoon, Exploring anomalous charge storage in anode materials for next-generation Li rechargeable batteries, Chem. Rev. 120 (2020) 6934–6976.

[48] Y. Li, Y. Huang, Y. Zheng, R. Huang, J. Yao, Facile and efficient synthesis of α-Fe_2O_3 nanocrystals by glucose-assisted thermal decomposition method and its application in lithium ion batteries, J. Power Sources 416 (2019) 62–71.

[49] H.S. Jadhav, R.S. Kalubarme, C.-N. Park, J. Kim, C.-J. Park, Facile and cost effective synthesis of mesoporous spinel $NiCo_2O_4$ as an anode for high lithium storage capacity, Nanoscale 6 (2014) 10071–10076.

[50] Y. Zheng, Y. Li, R. Huang, Y. Huang, J. Yao, B. Huang, A.A. Dubale, Fabrication of 2D NiO porous nanosheets with superior lithium storage performance via a facile thermal-decomposition method, ACS Appl. Energy Mater. 2 (2019) 8262–8273.

[51] J. Cabana, L. Monconduit, D. Larcher, M.R. Palacin, Beyond intercalation-based Li-ion batteries: the state of the art and challenges of electrode materials reacting through conversion reactions, Adv. Mater. 22 (2010) E170–E192.

[52] T.L. Nguyen, D.S. Kim, J. Hur, M.S. Park, I.T. Kim, Ni-Sn-based hybrid composite anodes for high-performance lithium-ion batteries, Electrochim. Acta 278 (2018) 25–32.

[53] T.L. Nguyen, J. Hur, I.T. Kim, Facile Synthesis of quantum dots SnO_2/Fe_3O_4 hybrid composites for superior reversible lithium-ion storage, J. Ind. Eng. Chem. 72 (2019) 504–511.

[54] L. Zhang, P. Hu, X. Zhao, R. Tian, R. Zou, D. Xia, Controllable synthesis of core–shell Co@CoO nanocomposites with a superior performance as an anode material for lithium-ion batteries, J. Mater. Chem. 21 (2011) 18279–18283.

[55] C. Kim, J.-W. Jung, K.R. Yoon, D.-Y. Youn, S. Park, I.-D. Kim, A high-capacity and long-cycle-life lithium-ion battery anode architecture: silver nanoparticle-decorated SnO_2/NiO nanotubes, ACS Nano 10 (2016) 11317–11326.

[56] L. Wang, X. Xie, K.N. Dinh, Q. Yan, J. Ma, Synthesis, characterizations, and utilization of oxygen-deficient metal oxides for lithium/sodium-ion batteries and supercapacitors, Coord. Chem. Rev. 397 (2019) 138–167.

[57] G. Zhang, T. Xiong, M. Yan, L. He, X. Liao, C. He, C. Yin, H. Zhang, L. Mai, $\alpha\text{-}MoO_{3-x}$ by plasma etching with improved capacity and stabilized structure for lithium storage, Nano Energy 49 (2018) 555–563.

[58] R. Wei, Y. Lu, Y. Xu, The role of oxygen vacancies in metal oxides for rechargeable ion batteries, Sci. China Chem. 64 (2021) 1826–1853.

[59] Q. Hu, B. Yue, H. Shao, F. Yang, J. Wang, Y. Wang, J. Liu, Facile syntheses of perovskite type $LaMO_3$ (M= Fe, Co, Ni) nanofibers for high performance supercapacitor electrodes and lithium-ion battery anodes, J. Alloys Compd. 852 (2021), 157002.

[60] M. Xuan Tran, J.-Y. Woo, T.-A. Nguyen, S.-W. Lee, J. Kee Lee, Thermolytically grafted silicon particles with ultrathin carbonaceous coating rich of phenyl moieties as lithium-storage anode material, Chem. Eng. J. 395 (2020), 125169.

[61] Z.-J. Zhang, Y.-X. Wang, S.-L. Chou, H.-J. Li, H.-K. Liu, J.-Z. Wang, Rapid synthesis of $\alpha\text{-}Fe_2O_3/rGO$ nanocomposites by microwave autoclave as superior anodes for sodium-ion batteries, J. Power Sources 280 (2015) 107–113.

[62] T.-A. Nguyen, S.-W. Lee, Green synthesis of N-doped carbon modified iron oxides ($N\text{-}Fe_2O_3$@Carbon) using sustainable gelatin cross-linker for high performance Li-ion batteries, Electrochim. Acta 248 (2017) 37–45.